Unsteady aerodynamic forces and torques on falling parallelograms in coupled tumbling-helical motions

Kapil Varshney,[1,*] Song Chang,[2,*] and Z. Jane Wang[3,4,*,†]
[1]*Taitem Engineering, PC, Ithaca, New York 14850, USA*
[2]*School of Applied and Engineering Physics, Cornell University, Ithaca, New York 14853, USA*
[3]*Sibley School of Mechanical and Aerospace of Engineering, Cornell University, Ithaca, New York 14853, USA*
[4]*Department of Physics, Cornell University, Ithaca, New York 14853, USA*
(Received 4 February 2013; published 29 May 2013)

Falling parallelograms exhibit coupled motion of autogyration and tumbling, similar to the motion of falling tulip seeds, unlike maple seeds which autogyrate but do not tumble, or rectangular cards which tumble but do not gyrate. This coupled tumbling and autogyrating motion are robust, when card parameters, such as aspect ratio, internal angle, and mass density, are varied. We measure the three-dimensional (3D) falling kinematics of the parallelograms and quantify their descending speed, azimuthal rotation, tumbling rotation, and cone angle in each falling. The cone angle is insensitive to the variation of the card parameters, and the card tumbling axis does not overlap with but is close to the diagonal axis. In addition to this connection to the dynamics of falling seeds, these trajectories provide an ideal set of data to analyze 3D aerodynamic force and torque at an intermediate range of Reynolds numbers, and the results will be useful for constructing 3D aerodynamic force and torque models. Tracking these free falling trajectories gives us a nonintrusive method for deducing instantaneous aerodynamic forces. We determine the 3D aerodynamic forces and torques based on Newton-Euler equations. The dynamical analysis reveals that, although the angle of attack changes dramatically during tumbling, the aerodynamic forces have a weak dependence on the angle of attack. The aerodynamic lift is dominated by the coupling of translational and rotational velocities. The aerodynamic torque has an unexpectedly large component perpendicular to the card. The analysis of the Euler equation suggests that this large torque is related to the deviation of the tumbling axis from the principle axis of the card.

DOI: 10.1103/PhysRevE.87.053021 PACS number(s): 47.85.Gj, 47.80.Jk

I. INTRODUCTION

A falling object moving through a viscous liquid exhibits rich dynamics of both theoretical and practical interests in engineering, meteorology, biomechanics, and ecology. The falling dynamics of seeds are critical for understanding their dispersal properties. Many single or multiple-winged seeds exhibit complex aerial movements which assist their long distance propagation [1–3]. The tropical seeds exhibit at least four different types of falling: autogyration, rolling gyration, floating, and undulation [1]. In our previous work, we found that the autorotation of maple samaras resulted from a subtle coupling between the rigid body dynamics and aerodynamics [4]. Unlike maple samaras, tulip seeds autogyrate while tumbling along their spanwise direction [5]. One key difference between the two cases is the mass distribution. In the case of a maple samara, the nut is at the end of the wing whereas in the case of a tulip seed, the mass distribution is relatively uniform. Aerodynamics of falling seeds have been studied in laboratories where the kinematics and the flows are quantified [4–8].

To study the coupled dynamics of the autogyration and tumbling as seen in tulip seeds, we choose the parallelogram, one of the simplest shapes that exhibit the similar falling behavior. The simplicity of the parallelogram gives us a handle to systematically vary its geometry, thereby allowing us to investigate a family of motions. This will complement the existing rich literature on free-falling objects and flapping wings (Table I) [9–38].

In addition to this connection to the dynamics of falling seeds, these trajectories provide an ideal set of data to analyze three-dimensional (3D) aerodynamic force and torque at an intermediate range of Reynolds numbers, and the results will be useful for constructing 3D aerodynamic force and torque models. Tracking these free falling trajectories gives us a nonintrusive method for deducing instantaneous aerodynamic forces. This was introduced in the studies of two-dimensional (2D) rectangular falling plates in water [21,27]. In this study we extend the analysis to 3D kinematics to extract 3D aerodynamic forces and torques. In what follows, we report detailed measurements of the kinematics and aerodynamic forces of the falling parallelograms by varying parameters, such as mass density, aspect ratio, and internal angle. The experimental aerodynamic forces and torques may guide future development of 3D aerodynamic models of falling objects.

II. EXPERIMENTAL APPARATUS AND MEASUREMENT PROCEDURE

The experiments are performed in still air. A schematic diagram of the experimental setup and arrangement of the apparatus are shown in Fig. 1. In this study, flat, parallelogram shaped, white cards of length L, width W, thickness d (with $d \ll [W,L]$), and internal angle γ are dropped in still air with their long axis horizontal and acute axis vertical from an approximate height of 1.5 m. The long axis is parallel to the card length and passes through the center of mass, and the acute axis is perpendicular to the long axis and also passes through

*All authors contributed equally to this work.
†Author for correspondence: jane.wang@cornell.edu

TABLE I. A summary of previous investigations on freely falling objects, fixed axis autorotation, and flapping motion.

References	Object	Free fall/ fixed axis	Aspect ratio	Fluid	Motion observed	Re
			(a) Experimental Studies			
Varshney *et al*. [4]	Maple seeds	Free fall		Air	Autogyrating motion	10^3
McCutchen [5]	Tulip seeds	Free fall		Air	Coupled tumbling-autogyrating motion	
Norberg [7]	Maple seeds	Free fall		Air	Autogyrating motion	10^3
Lentink *et al*. [8]	Maple seeds	Free fall		Mineral oil	Autogyrating motion	10^3
Lugt [11]	Various bodies	Free/fixed		Air		
Smith [12]	Rectangular plate	Fixed axis	3 to 4	Air/water	Autorotation	10^4 to 3×10^5
	Rectangular plate	Free fall	3 to 4	Air	Tumbling	10^2 to 10^4
Skews [14]	Polygonal bodies	Fixed axis		Air	Autorotation	10^4 to 10^5
Ozen & Rockwell [15]	Rectangular plate	Fixed axis		Mineral oil	Flapping wing	
Riabouchinsky [16]	Rectangular card	Free fall		Air	Fluttering/tumbling	
Willmarth *et al*. [17]	Circular disk	Free fall	1	Glycol/water	Fluttering/chaotic/ steady descent	10^2 to 10^3
Field *et al*. [18]	Circular disk	Free fall	1	Glycol/water	Fluttering/chaotic/ tumbling	10^2 to 10^4
Mahadevan *et al*. [19]	Rectangular card	Free fall	5	Air	Tumbling	
Belmonte *et al*. [20]	Rectangular plate	Free fall	1 to 42	Glycerol/water	Fluttering/tumbling	10^2 to 10^3
Andersen *et al*. [21]	Rectangular plate	Free fall	15 to 30	Water	Fluttering/chaotic/ tumbling	10^2 to 10^3
Dickinson *et al*. [22]	Robotic wing	Fixed axis		Mineral oil	Wing rotation	$<10^3$
Ellington *et al*. [23]	Robotic wing	Fixed axis		Air	Flapping wing	10^2 to 10^3
Bomphrey *et al*. [24]	Robotic wing	Fixed axis		Air	Flapping wing	
			(b) Numerical studies			
Pesavento & Wang [25]	Falling paper	Free fall	8		Fluttering/tumbling	10^3
Jones & Shelley [26]	Flat plate	Free fall				10^2 to 10^3
Andersen *et al*. [27]	Rectangular plate	Free fall	15 to 30		Fluttering/tumbling	400 to 600
Mittal *et al*. [28]	Cylinder	Free fall			Fluttering/tumbling	10^2
Jin & Xu [29]	Plates	Free fall	8		Fluttering/tumbling	837 to 1100

the center of mass. The card parameters, such as aspect ratio L/W, internal angle γ, and mass density ρ_s, can influence the falling trajectory. We vary those parameters systematically and analyzed 84 different cases in total. The aspect ratio is altered from 1.5 to 5, with the card thickness and width fixed ($d \backsim 0.2$ mm, $W = 1$ cm), and the card length varied from 1.5 to 5 cm. In another set of experiments, the internal angle of the parallelogram is changed from 15° to 85° in steps of 5°, while the aspect ratio is fixed at 4. Lastly, we vary the density of the card in a four-fold change while keeping the aspect ratio at 4 and the internal angle at 45°.

Other parameters which influence the dynamics of the cards in question are the mass density of the card $\rho_s = 1.2 \times 10^3$ kg/m^3, the density of air $\rho_a = 1.23$ kg/m^3, the gravitational acceleration $g = 9.8$ m/s^2, and the dynamic viscosity of air $\mu = 1.73 \times 10^5$ (N-s/m^2). Four dimensionless parameters relevant in this analysis are the Reynolds number $\mathrm{Re} = \rho_a \Omega w^2/\mu$, the aspect ratio L/W, the buoyancy number $\rho_s/\rho_a - 1$, and the thickness-to-width ratio of the card, d/W. The last two can be combined to obtain the dimensionless moment of inertia $I^* = \sqrt{\frac{\rho_s d}{\rho_a W}}$.

In Fig. 1, the experimental apparatus includes a high-speed camera (Vision Research, Phantom v5.0), a mirror of size 76 × 51 cm which is mounted at 45° from the horizontal, and two black backgrounds of which one is placed on the opposite side of the mirror and the other is placed horizontally at 2 m above the mirror. Both backgrounds are illuminated homogeneously to obtain good contrast. The sampling rate needs to be sufficient to enable our subsequent analysis of the card kinematics. Our results indicate that 1000 frames/s were sufficient to resolve the motion of the card, and therefore the trajectories of the falling cards are recorded at this frame rate. To capture the time dependent card motions with 6 degrees of freedom, top and side views of the free falling cards are recorded using a single high-speed video camera. A detailed description of the experimental setup has been reported elsewhere [4].

We carry out a calibration to determine the instantaneous size of the card, since the size of the card image is a function of the distance from the camera lens. Two calibrations, one for the side view and the other for the top view, have been performed. An orthogonal grid of 1 × 1 cm square lines is plotted on a sheet of paper. For the top view, the sheet is positioned horizontally and moved up in the Z axis to eight known distances, 37.5 cm in total, from the top edge of the mirror and moved down in the Z axis to three known distances, 13.2 cm in total, from the top edge of the mirror. For the side view, the sheet was positioned vertically and then moved horizontally to seven known distances, 30 cm in total. In our experiments, we record videos of the card motion when the

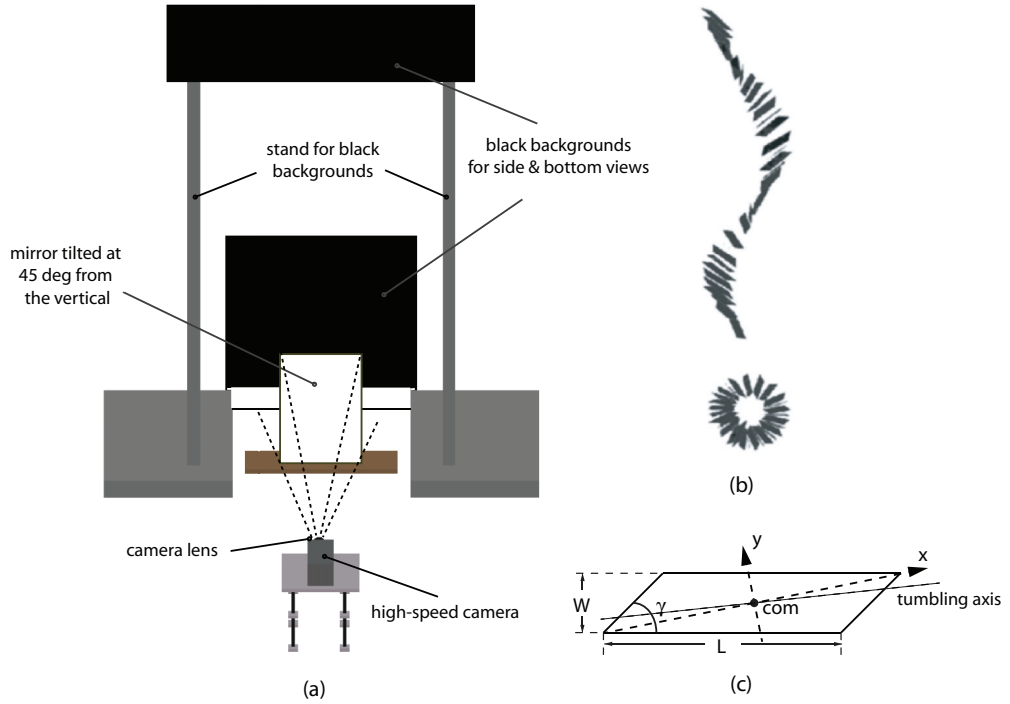

FIG. 1. (Color online) (a) Experimental apparatus. (b) Sampled images of falling parallelograms. The two views show that the card tumbles and falls in the shape of a helix. (c) A parallelogram and its length L, width W, internal angle γ, center of mass (com), diagonal axis x, chord axis y, and tumbling axis (schematic).

falling is within the calibrated region. All experiments are performed in a closed laboratory to prevent any unwanted airflow.

III. KINEMATICS OF THE PARALLELOGRAMS

Figure 2 shows a reconstruction of the card falling in 3D space. The card tumbles while its center of mass falls along a vertical helix. In all experiments, the cards settle into a stable tumbling motion quickly. Fluttering or chaotic motions are not observed. We suspect that this is likely a result of the limited range of the dimensionless moment of inertia I^* which is critical in determining the transition between different types of falling [17,18,21,27]. The card tumbling frequency is $\backsim$16 Hz, and the Reynolds number Re is of the order of 10^3. The tumbling frequency of the card is one order of magnitude higher than the gyration frequency. During the descent, the parallelograms maintain a steady cone angle for all captured cases.

The position of the center of mass and three Euler angles were tracked throughout the descent of the cards. As shown in Fig. 3, "XYZ" is the laboratory frame, in which "X" and "Y" form a horizontal plane, and "Z" corresponds to a vertical axis. "xyz" is the card frame with "x" the diagonal axis, "y" the chord direction, and "z" normal to the card plane. In this analysis, the Euler angles are (1) azimuthal angle ϕ about the Z axis, (2) tilting angle θ about the rotated Y axis, and (3) pitching angle ψ about the long diagonal axis of the card (Fig. 3). The tip of the card traces out a cone whose angle is $90^\circ - |\theta|$.

Figure 4 shows the time series of velocities and angular velocities for the card in Fig. 2. The numerical differentiations are computed through a robust locally weighted regression method [39]. In this case, the terminal velocity remains approximately constant. The azimuthal velocities, V_x and V_y, are two orthogonal components of the circular motion. There is a small drift associated with the tilt of the cone angle, which is estimated to be 3°.

The spanwise component of the angular velocity, ω_x, remains constant. We observe that the axis of tumbling is neither the diagonal axis nor the long axis. Instead, the card tumbles about an axis that is about 4.6° away from the diagonal axis. In Fig. 4(b), the angular velocities have been computed with respect to the body frame of the card. The oscillations seen in ω_y and ω_z are due to the tumbling motion of the card.

We varied parameters of the card, such as aspect ratio (1.5 to 5), mass density (a factor of 4 change), and internal angle (15° to 88°), and analyzed a total of 86 kinematics. In all cases, the cards fall in the shape of a helix, and the cone angle is insensitive to the parameters and approximately 55°. Tumbling velocity also does not alter with respect to either the aspect ratio or the internal angles; however it increases with an increase in card density. The falling speed decreases with the aspect ratio but increases with the card density and is insensitive to the internal angles. In addition, we examine the variations of the cone angle and the gyration radius when the internal angle of the card is changed and the aspect ratio is fixed at AR = 4 (Fig. 5). The internal angle is varied from 15° to 85° with increments of 5°, as well as two samples at 82° and 88° for near-rectangular cards. Throughout the range of parameters we study, the cone angle varies with one standard deviation equal to 5.9°, which is comparable to the uncertainty of the measurement, ±3°. However, we note an increase in the

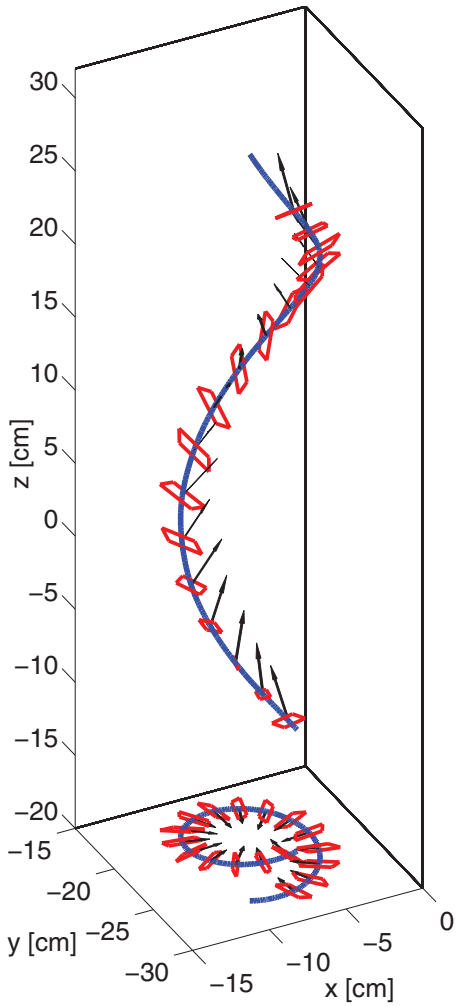

FIG. 2. (Color online) 3D reconstruction of a falling parallelogram card with an aspect ratio at 4 and an internal angle at 45°. The arrows show the directions and magnitudes of aerodynamic forces at various locations during the descent. The projection of the trajectory onto an x-y plane shows the helical configuration.

gyration radius when the internal angle increases above 70°. On average, the gyration radii are 5.9 and 15.2 cm for the internal angle of the card below and above 80°, respectively.

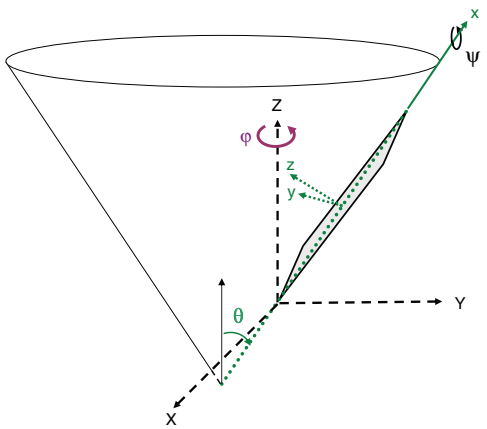

FIG. 3. (Color online) The Euler angles and the frames of reference. XYZ is the laboratory frame, and xyz is the card frame.

This difference is systematic and not due to the uncertainty in our length measurement. This increase in the gyration radius signifies a transition in the falling behavior.

We might further expect that, as its internal angle approaches 90°, a rectangular card would tumble about its spanwise axis and fall in a two-dimensional motion. It turns out that tumbling motion is only a transient during the fall for cards of finite span. After its initial tumbling, a card tilts and gyrates. To investigate this transition, we have examined parallelograms with different combinations of aspect ratio and internal angle close to 90°. All cards tumble initially and gradually transition into a helixlike motion. The helical motion is not always stable and the cards can fall erratically. The transition from tumbling to gyration is initialized by a tilt about the shorter axis of the card, and the tilt is caused by the aerodynamic torque due to the offset of the center of the pressure away from the center of mass. By Euler's equations for a rigid body, the coupling between the tumbling motion about the span axis and the tilt about the intermediate axis will lead to gyration.

The time scale associated with the transition from tumbling to gyrating motion depends on the magnitude of the aerodynamic torque and the moment of inertia. The aerodynamic force grows with falling speed, the offset between the center of pressure and the center of mass decreases as the card approaches to rectangular shape, and the moment of inertia increases as the span increases. Therefore, among cards of the same aspect ratio, the ones with larger internal angles have a longer transition time. Among cards of the same internal angle, the ones with larger span have a longer transition time. In previous experiments of tumbling aluminum plates in water, the span is about 30 times the width, and the tilting time is much longer than the time window of observation [21]. For the current cards, we are limited with the range of span because of the flexibility of the paper, and we have focused on cards whose span to chord ratio is below 10. In these cases, the cards always transition into a gyrating motion. We expect that the pure two-dimensional motion occurs only in cards of infinite span.

IV. DYNAMICAL ANALYSIS

The 3D kinematics of a free-falling object in a fluid is sufficient for us to deduce the unsteady aerodynamic forces and torques on the object. To extract the instantaneous forces and torques experienced by the falling parallelograms, we calculate the accelerations from the kinematic data and then apply the Newton-Euler equations,

$$\vec{F}^a = m\vec{a} - m\vec{g}, \quad \vec{\tau}^a = \mathbf{I}\vec{\beta} + \vec{\omega} \times (\mathbf{I}\vec{\omega}).$$

Here $\vec{F}^a$ and $\vec{\tau}^a$ are the aerodynamic forces and torques, respectively, m is the card mass, $\mathbf{I}$ is the moment of inertia, $\vec{\beta}$ is the angular acceleration, $\vec{\omega}$ is the angular velocity, and $\vec{g}$ is the gravity. Second order derivatives of the kinematic data are computed numerically using the robust locally weighted regression method [39].

The time series of aerodynamic forces are shown in Fig. 6(a) (laboratory frame) and Fig. 6(b) (local body frame) for the card in Fig. 2. In the laboratory frame, F_X and F_Y are components of the centrifugal force, and F_Z balances the gravity in steady

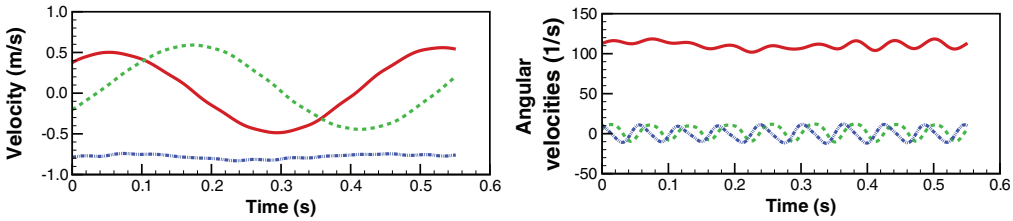

FIG. 4. (Color online) (a) 3D velocities of the falling parallelogram in steady states: V_X (solid red), V_Y (dashed green), and V_Z (dotted dashed blue). (b) Time series of angular velocities: ω_x (solid red), ω_y (dashed green), and ω_z (dotted dashed blue).

falling. The force decomposition in the body frame shows a small component along the diagonal axis, indicating that the force is almost normal to this axis. The oscillation seen in F_y and F_z are due to the card tumbling. The oscillation frequency is approximately 15.8 Hz, which is the same as the tumbling frequency.

To study the dependence of aerodynamic forces on the card kinematics, we compare the following vectors in Fig. 6(c): the aerodynamic forces (black), the linear velocities (green), the angular velocities (red), the card normal vectors (yellow), and the cross product (blue) of card angular velocities with linear velocities. We remove the gyration and the descending motion and only render the tumbling of the card. The geometric angle of attack is the angle between the linear velocity and card plane. Although the angle of attack changes dramatically within one tumbling period, the aerodynamic forces have a weak dependence on the angle of attack, indicating that the aerodynamic lift is dominated by the coupling of translational and angular velocities.

To examine the dependence of the aerodynamic forces on the linear and the angular velocities (v and ω), we decompose the total aerodynamic forces [Fig. 6(d)] into following directions: (1) $-\hat{u}$ (the drag), (2) $\hat{\omega}\times\hat{u}$ (the rotational lift), and (3) $(\hat{\omega}\times\hat{u})\times\hat{u}$ (the remaining lift),

$$\vec{F}^a = \tfrac{1}{2}\rho_f U^2 A[C_d(-\hat{u}) + C_{L1}(\hat{\omega}\times\hat{u}) + C_{L2}(\hat{\omega}\times\hat{u})\times\hat{u}],$$

where ρ_f is the air density, U is the velocity scale, A is the area of the card, and C_d, C_{L1}, and C_{L2} are the dimensionless force coefficients.

During the descent, the force coefficients have small oscillations at the tumbling frequency [Fig. 6(e)]. On average, $\overline{C}_d = 1.06$, $\overline{C}_{L1} = 0.92$, and $\overline{C}_{L2} = 0.32$. The force is dominated by the aerodynamic drag and the lift along the direction of $\hat{\omega}\times\hat{u}$, and the remaining lift component F_{L2} on average accounts for only 28% of the total aerodynamic forces. C_d and C_{L1} can be viewed as constants with modulations due to tumbling. Further analyzes of these forces will be instructive for constructing a 3D quasisteady aerodynamic model for falling objects.

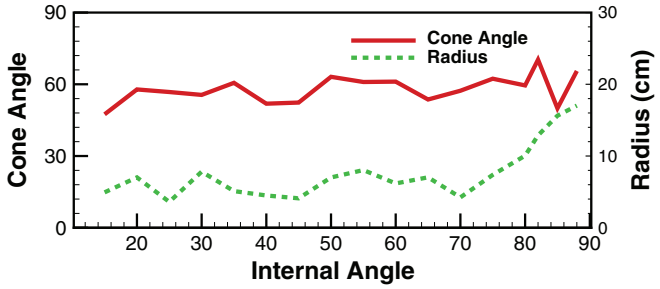

FIG. 5. (Color online) Dependence of the internal angle on the cone angle and the radius of gyration of a falling parallelogram card for a fixed aspect ratio at 4.

The time series of aerodynamic torques are displayed in Fig. 6(f). Three components oscillate at twice the tumbling frequency due to the π-rotational symmetry of the card about the diagonal axis. Incidentally, this symmetry breaks down in the forces because of the gravity. We note that τ_z is much greater than τ_x and τ_y. To understand this phenomenon, we carry out a scaling analysis based on the Euler equations. To simplify the derivation, we describe the card motion using the tumbling axis, and thus the gyration rate ω_ϕ, the tumbling rate ω_ψ, and the cone angle θ_0 are taken to be constants. The angular velocities in the body frame are

$$\omega_x = \omega_\psi + \omega_\phi\cos\theta_0, \quad \omega_y = (\omega_\phi\sin\theta_0)\sin(\omega_\psi t),$$
$$\omega_z = (\omega_\phi\sin\theta_0)\cos(\omega_\psi t).$$

Because of our choice of axes, the moment of inertia tensor has one off-diagonal, I_{xy}. The aerodynamic torques can be deduced from the Euler equations,

$$\frac{\tau_x}{I_x\omega_\phi^2} = \frac{1}{2}\sin^2\theta_0\sin(2\omega_\psi t) - \frac{I_{xy}}{I_x}\frac{\omega_\psi}{\omega_\phi}\sin\theta_0\cos(\omega_\psi t),$$
$$\frac{\tau_y}{I_x\omega_\phi^2} = -\frac{I_y}{2I_x}\sin 2\theta_0\cos(\omega_\psi t) + \frac{I_{xy}}{2I_x}\sin^2\theta_0\sin(2\omega_\psi t),$$
$$\frac{\tau_z}{I_x\omega_\phi^2} = -\frac{2\omega_\psi}{\omega_\phi}\sin\theta_0\sin\omega_\psi t + \left(\frac{I_y}{2I_x}\sin 2\theta_0\right)\sin(\omega_\psi t) + \frac{I_{xy}}{I_x}\left[\left(\frac{\omega_\psi}{\omega_\phi}\right)^2 - \sin^2\theta_0\sin^2(\omega_\psi t)\right],$$

where the torques are normalized by $I_x\omega_\phi^2$. These equations take into account the fact that ω_ψ is roughly an order of magnitude greater than ω_ϕ.

For the parallelogram shown in Fig. 2, the moments of inertia have the following relative magnitudes: $I_x : I_{xy} : I_y : I_z \sim 1 : 2 : 10 : 11$. Replacing the ratios in the equations by these approximated values and taking $\theta_0 \sim 55^\circ$, we find (1) τ_x, τ_y, and τ_z are oscillations with frequency $2\omega_\psi$, with τ_x and τ_y averaged to zero; (2) τ_x is dominated by the second term; (3) τ_y has two comparable terms, with the first slightly greater; and (4) τ_z, unlike the other two components, contains a nonzero constant term, $\frac{I_{xy}}{I_x}(\frac{\omega_\psi}{\omega_\phi})^2$, which is an order of magnitude greater than the amplitude of the oscillation seen in the first term. This large offset in τ_z is seen in Fig. 6(f). It is associated with the large ratio $\frac{\omega_\psi}{\omega_\phi}$ and the nonzero I_{xy}. While

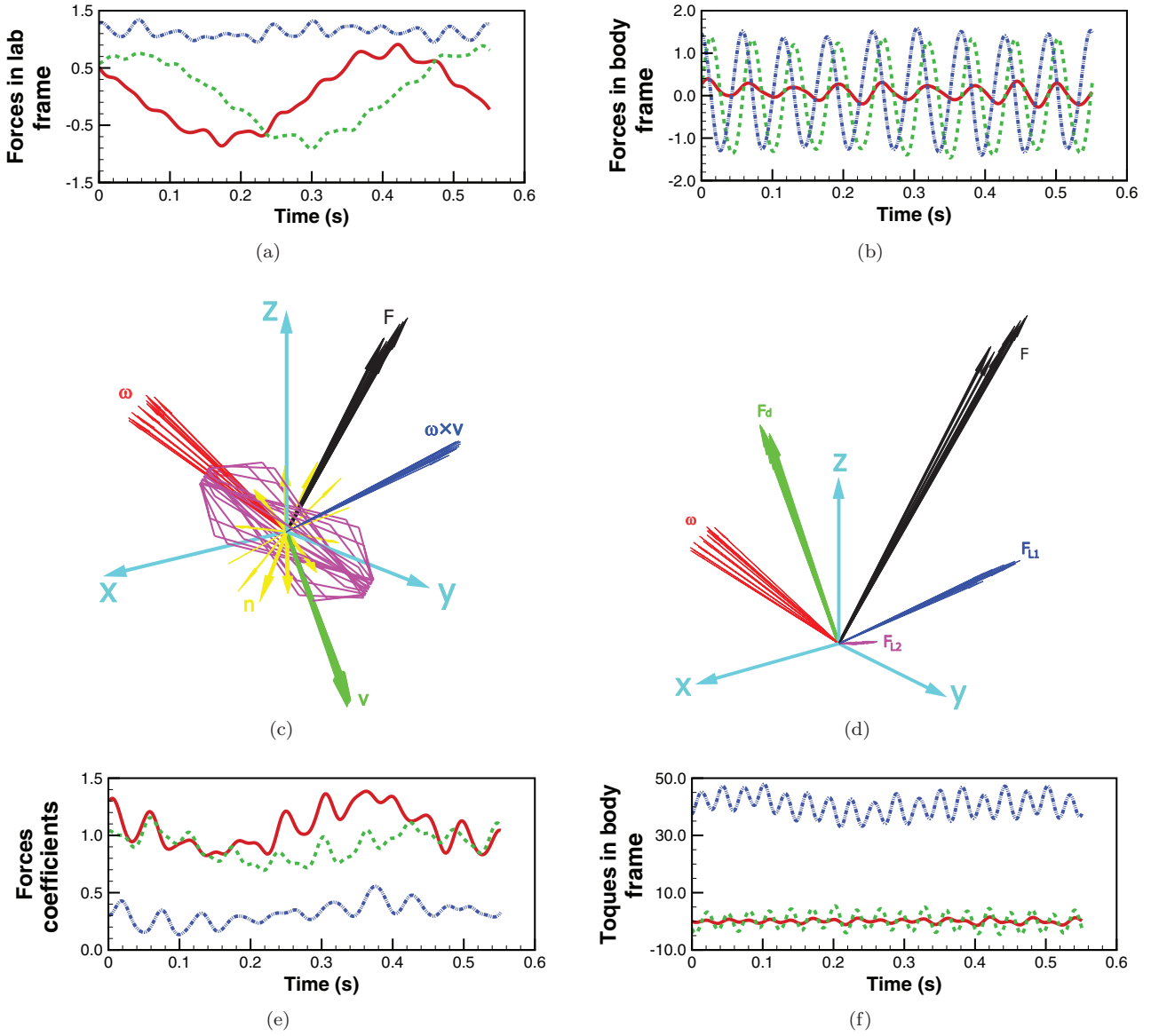

FIG. 6. (Color online) (a) and (b) Time series of aerodynamic forces. (a) Forces in laboratory frame: F_X (solid red), F_Y (dashed green), and F_Z (dotted dashed blue). (b) Forces in card body frame: F_x (solid red), F_y (dashed green), and F_z (dotted dashed blue). (c) and (d) Aerodynamic force (black) diagrams during one tumbling period. (c) Linear velocities (green), angular velocities (red), cross product of linear and angular velocities (blue), card normals (yellow), and card plane (magenta). (d) Aerodynamic drag (green), rotational lift (blue), and remaining lift (magenta). (e) Time series of three force coefficients: C_d (solid red), C_{L1} (dashed green), and C_{L2} (dotted dashed blue). (f) Time series of aerodynamic torques in body frame: τ_x (solid red), τ_y (dashed green), and τ_z (dotted dashed blue).

the former is an intrinsic nature of falling parallelograms, the nonzero I_{xy} resulted from the deviation of the tumbling axis from the principle axis which is very close to the long axis for the card shown here. The large τ_z must result from the aerodynamic force tangential to the plane. Noting that the force in the spanwise direction of the card is small [Fig. 6(b)], the tangential force primarily lies in the direction of the chord along the short axis of the card.

V. CONCLUSIONS AND DISCUSSIONS

Our experiments and analysis have focused on the kinematics and unsteady aerodynamic forces of free falling parallelograms in still air. We observe that the cards exhibit simultaneous tumbling and helical motions during their descent. This resembles the motion of falling tulip seeds. During the descent, the card has negligible horizontal drift and maintains a steady cone angle. The card tumbling is around an axis between the diagonal and the long axes. The analysis result shows that the tumbling frequency is one order of magnitude higher than that of the gyration frequency.

We use the falling kinematics to deduce the aerodynamic forces and torques experienced by the parallelograms. To extract the instantaneous forces and torques, we calculate the accelerations from the kinematic data and then applied the Newton-Euler equations. The analyzes show that, regardless

of the drastic change in the geometric angle of attack during tumbling periods, the magnitude and direction of the aerodynamic forces maintain nearly steady. This suggests that the forces depend on the card translational velocity and angular velocity which are also nearly constant during the tumbling. The large torque about the card normal is contributed by the tangential force that primarily lies in the direction of the card chord.

[1] C. K. Augspurger, Amer. J. Bot. **73**, 353 (1986).
[2] R. Nathan, G. G. Katul, H. S. Horn, S. M. Thomas, R. Oren, R. Avissar, S. W. Pacala, and S. A. Levin, Nature **418**, 409 (2002).
[3] R. Nathan, Science **313**, 786 (2006).
[4] K. Varshney, S. Chang, and Z. J. Wang, Nonlinearity **25**, C1 (2012).
[5] C. W. McCutchen, Science **197**, 691 (1977).
[6] K. Yasuda and A. Azuma, J. Theor. Biol. **185**, 313 (1997).
[7] R. A. Norberg, Bio. Rev. **48**, 561 (1973).
[8] D. Lentink, W. B. Dickson, J. L. van Leeuwen, and M. H. Dickinson, Science **324**, 1438 (2009).
[9] J. C. Maxwell, Camb. Dublin Math. J. **9**, 115 (1854).
[10] P. Dupleich, NACA Technical Mem. **1201**1 (1941).
[11] H. J. Lugt, Annu. Rev. Fluid Mech. **15**, 123 (1983).
[12] E. H. Smith, J. Fluid Mech. **50**, 513 (1971).
[13] B. W. Skews, Nature (London) **352**, 512 (1991).
[14] B. W. Skews, J. Fluid Mech. **217**, 33 (1990).
[15] C. A. Ozen and D. Rockwell, Exp. Fluids **50**, 23 (2011).
[16] D. P. Riabouchinsky, London: R. Aeronaut. Soc. **77**, 283 (1935).
[17] W. W. Willmarth, N. E. Hawk, and R. L. Harvey, Phys. Fluids **7**, 197 (1964).
[18] S. B. Field, M. Klaus, M. G. Moore, and F. Nori, Nature (London) **388**, 252 (1997).
[19] L. Mahadevan, W. S. Ryu, and A. D. T. Samuel, Phys. Fluids **11**, 1 (1999).
[20] A. Belmonte, H. Eisenberg, and E. Moses, Phys. Rev. Lett. **81**, 345 (1998).
[21] A. Andersen, U. Pesavento, and Z. J. Wang, J. Fluid Mech. **541**, 65 (2005).
[22] M. H. Dickinson, F. O. Lehmann, and S. P. Sane, Science **284**, 1954 (1999).
[23] C. P. Ellington, C. van den Berg, and A. P. Willmott, Nature (London) **384**, 626 (1996).
[24] R. J. Bomphrey, G. K. Taylor, and A. L. R. Thomas, Exp. Fluids **46**, 811 (2009).
[25] U. Pesavento and Z. J. Wang, Phys. Rev. Lett. **93**, 144501 (2004).
[26] M. A. Jones and M. J. Shelley, J. Fluid Mech. **540**, 393 (2005).
[27] A. Andersen, U. Pesavento, and Z. J. Wang, J. Fluid Mech. **541**, 91 (2005).
[28] R. Mittal, V. Seshadri, and H. S. Udaykumar, Theor. Comput. Fluid Dyn. **17**, 165 (2004).
[29] C. Jin and K. Xu, Commun. Comput. Phys. **3**, 834 (2008).
[30] Y. Tanabe and K. Kaneko, Phys. Rev. Lett. **73**, 1372 (1994).
[31] L. Mahadevan, C. R. Acad. Sci. Ser. IIb **323**, 729 (1996).
[32] M. A. Jones, J. Fluid Mech. **496**, 405 (2003).
[33] K. Namkoong, J. Y. Yoo, and H. G. Choi, J. Fluid Mech. **604**, 33 (2008).
[34] Z. J. Wang, Annu. Rev. Fluid Mech. **37**, 183 (2005).
[35] C. Hsieh, C. C. Chang, and C. C. Chu, J. Fluid Mech. **623**, 121 (2009).
[36] K. Varshney, *Doctoral Dissertations for UMass Amherst*, Paper AAI3372281 (2009).
[37] A. J. Bergou, L. Ristroph, J. Guckenheimer, I. Cohen, and Z. J. Wang, Phys. Rev. Lett. **104**, 148101 (2010).
[38] P. Ern, F. Risso, D. Fabre, and J. Magnaudet, Annu. Rev. Fluid Mech. **44**, 97 (2012).
[39] W. S. Cleveland, J. Am. Stat. Assoc. **74**, 829 (1979).